

## Article

# Oxide Nanostructured Coating for Power Lines with Anti-Icing Effect

Andrey Vladimirovich Blinov<sup>1</sup>, Dmitry Aleksandrovich Kostyukov<sup>1</sup>, Maria Anatolevna Yasnaya<sup>1</sup>, Pavel Aleksandrovich Zvada<sup>1</sup>, Lyudmila Pavlovna Arefeva<sup>2</sup>, Valery Nikolaevich Varavka<sup>2</sup>, Roman Aleksandrovich Zvezdilin<sup>1</sup>, Alexander Aleksandrovich Kravtsov<sup>1,3</sup>, David Guramievich Maglakelidze<sup>1</sup>, Alexey Borisovich Golik<sup>1</sup>, Alexey Alekseevich Gvozdenko<sup>1</sup>, Natalia Viatcheslavovna Lazareva<sup>4</sup>, Elena Nikolaevna Kushch<sup>4</sup>, Vadim Nikolaevich Goncharov<sup>5</sup>, Maxim Andreevich Kolodkin<sup>1</sup>, Mohammad Ali Shariati<sup>6</sup> and Andrey Ashotovich Nagdalian<sup>1,7,\*</sup>

<sup>1</sup> Department of Physics and Technology of Nanostructures and Materials, North Caucasus Federal University, 355017 Stavropol, Russia

<sup>2</sup> Don State Technical University, 344000 Rostov-on-Don, Russia

<sup>3</sup> Federal Research Center the Southern Scientific Centre of the Russian Academy of Sciences, Chehova Street 41, 344006 Rostov-on-Don, Russia

<sup>4</sup> Economic Security and Auditing Department, North Caucasus Federal University, 355017 Stavropol, Russia  
<sup>5</sup> Department of Scientific Research, Technological Institute of Service—Branch of the Don State Technical University in Stavropol, 355000 Stavropol, Russia

<sup>6</sup> Department of Scientific Research, K.G. Razumovsky Moscow State University of Technologies and Management (The First Cossack University), 109004 Moscow, Russia

<sup>7</sup> Saint Petersburg State Agrarian University, 196601 Saint Petersburg, Russia

\* Correspondence: geniando@yandex.ru



**Citation:** Blinov, A.V.; Kostyukov, D.A.; Yasnaya, M.A.; Zvada, P.A.; Arefeva, L.P.; Varavka, V.N.; Zvezdilin, R.A.; Kravtsov, A.A.; Maglakelidze, D.G.; Golik, A.B.; et al. Oxide Nanostructured Coating for Power Lines with Anti-Icing Effect. *Coatings* **2022**, *12*, 1346. <https://doi.org/10.3390/coatings12091346>

Academic Editor: Jinyang Xu

Received: 26 July 2022

Accepted: 9 September 2022

Published: 16 September 2022

**Publisher's Note:** MDPI stays neutral with regard to jurisdictional claims in published maps and institutional affiliations.



**Copyright:** © 2022 by the authors. Licensee MDPI, Basel, Switzerland. This article is an open access article distributed under the terms and conditions of the Creative Commons Attribution (CC BY) license (<https://creativecommons.org/licenses/by/4.0/>).

**Abstract:** This paper presents the results of the development of a technology to obtain a nanostructured coating for the protection of overhead wires and the possibility of their application in the electric power industry. The paper provides an analysis of available data on methods of combating ice in different countries, ways to protect the surface of metals from environmental influences, and new materials used for protection. We studied the possibility of using a protective nanostructured coating to protect overhead wires. A technology for obtaining a protective nanostructured coating based on silicon oxide and methods for applying it to the wire of overhead lines are proposed. The analysis of the elemental composition and surface morphology of overhead line wires with protective coating is carried out by scanning electron microscopy. The influence of the nanostructured coating on the high-frequency signal bandwidth and wire resistance using a PCIe-6351 data acquisition board, equipped with a BNC-2120 terminal module generating a frequency signal were determined using the National Instruments LabVIEW software package. The subject of the study was a 110 kV overhead power line with a protective coating developed in this work. By analyzing the calculation, we obtained the operating requirements of the developed nanostructured coating. As a result, we developed a protective coating satisfying the working conditions and investigated its properties. In the final phase of the experiment, we tested the electrical characteristics of overhead wires with the developed protective coating.

**Keywords:** LabVIEW; nanostructured coating; overhead wires; superhydrophobic properties

## 1. Introduction

Electricity is an essential resource for a prosperous life. It is impossible to imagine our civilization without electricity: economic and social progress would be relegated to the past and our daily lives completely transformed. Electrical power has become universal. As we know, electricity is transmitted from power plants to homes by power lines; by wires. This poses a problem—in wet and cold regions of the world, where temperatures reach negative

values, wires become frosted, which leads to a decrease in electrophysical and mechanical properties and the breaking of power lines [1,2].

There are several solutions to solve this problem. For example, the most common one is to heat the wires using higher than the rated current (the Joule effect). The de-icing effect of power lines is achieved by a short-term increase in the current strength or a short-circuiting of the conductor [3,4].

In modern conditions, with an increasing trend towards general savings in the world, the heating of wires is an irrational waste of energy. In this case, it is necessary to seek other approaches for anti-icing. For example, the development of various kinds of protective coatings with hydrophobic properties. Wang et al. (2011) presented a study confirming the economic feasibility of using hydrophobic compositions to protect electrical wires from icing [5].

It is reported that the hydrophobic coating of the aluminum surface of power lines is not able to provide complete protection against ice formation, but significantly delays this process. Menini and Farzaneh (2009) demonstrated a successful surface treatment experience with an anti-icing coating based on poly(tetrafluoroethylene) [6]. The proposed compound provided a wetting contact angle up to  $140^\circ$ . The researchers were able to reduce the ice adhesion by 2.5 times and preserve the hydrophobic properties after several cycles of icing.

Protective coatings are thin films made of various chemical compounds. In particular, coatings based on  $\text{MnO}_2/\text{PS}$  composite (manganese oxide polystyrene),  $\text{ZnO}/\text{PS}$  composite (zinc oxide polystyrene),  $\text{CaCO}_3$  (precipitated calcium carbonate), as well as coatings based on carbon nanotubes, fluorinated silanes, fluoropolymer coatings,  $\text{SiO}_2$ , and composites with other oxides, etc. [7–17].

Of the compounds listed, coatings based on nanoscale oxide materials are the most promising. The anisotropic structure possessed by ceramic materials allows for the formation of strong protective coatings, which is why silicon dioxide-based coatings have received widespread recognition.  $\text{SiO}_2$  forms a relief structure with low surface energy, which contributes to the creation of a hydrophobic layer [18]. Ligang Xu and Junhui He obtained superhydrophobic coatings based on silicon oxide nanoparticles with a maximum wetting contact edge angle of  $156^\circ$  at a sliding angle of  $\leq 2^\circ$  and a maximum transmittance of 83.7% [19].

There are many methods to obtain silicon dioxide at the nanoscale: self-assembly method on a substrate [20], sonochemical method [21], magnetron sputtering method [22], and others [23,24]. Among all of the methods, the sol-gel method should be noted, which is economical, simple, and effective. Thus, it is possible to fine-tune the particle size during synthesis, to set the necessary porosity and, in particular, the surface energy [25].

However, to form a film with superhydrophobic properties, it is not enough to use only silicon dioxide. Many studies show that modification of  $\text{SiO}_2$  with other oxide particles, such as  $\text{TiO}_2$ ,  $\text{ZnO}$ ,  $\text{ZrO}_2$ ,  $\text{Fe}_2\text{O}_3$ , etc., is beneficial [26–30]. Therefore, the purpose of this work was to develop a technique to obtain a nanostructured oxide coating to protect power lines from icing, and investigate its elemental composition, morphology, structural and mechanical properties, and practical effectiveness. Consequently, the novelty of the work is associated with:

- (1) the use of nanostructured coating;
- (2) comparison of methods for obtaining a nanostructured coating;
- (3) determination of the optimal number of layers of nanostructured coating;
- (4) evaluation of the effect of nanostructured coating on the mechanical characteristics of power lines.

## 2. Materials and Methods

### 2.1. Materials

The following materials were used in the experiment: tetraethoxysilane (LLC “Silan”, Dankov, Russia), ethyl alcohol (LLC “Suvorovsky”, Stavropol, Russia), 25% ammonia

(LLC “Metachem”, Moscow, Russia), and distilled water. For the practical approval of the preparation, we used non-heat-treated aluminum alloy ABE (Table 1).

**Table 1.** Chemical composition of the electrical aluminum alloy of the AVE brand.

	Chemical Composition, %wt.							Tensile Strength, MPa
	Si	Fe	Cu	Mg	Zn	Ti, V, Cr, Mr	Al	
ABE	0.45–0.60	0.35–0.70	0.05	0.45–0.60	0.05	≈0.015	remaining portion	132–170

## 2.2. Synthesis and Technique of Applying a Protective Coating

In this work, we obtained a silicon oxide-based protective coating in two ways, depending on the application technique:

1. Application of SiO<sub>2</sub> nanoparticles sol to the surface of ABE wire. Synthesis of silicon oxide (SiO<sub>2</sub>) nanoparticles was carried out by the Stober method according to the following method [31]:

A total of 24 mL of distilled water and 65 mL of ethyl alcohol (96%) were injected into a 250 mL round-bottomed flask under constant stirring on a Heidolph MR Hei-Standard magnetic stirrer (“Heidolph Instruments” GmbH & CO. KG, Schwabach, Germany);

- (a) continued heating at 50 °C with the addition of 8 mL of 25% aqueous ammonia solution;
- (b) with constant stirring, 3 mL of tetraethoxysilane solution was slowly added dropwise,
- (c) the resulting sol was stirred for 1 h at 50 °C.

The ABE wire samples were immersed in this solution for 2 min and dried in a drying chamber Oven 125 (“IKA”, Staufen, Germany) at 150 °C for 10 min. After each drying, the mass of the obtained sample was measured. To apply the next layer, the operation was repeated. The number of layers varied from 1 to 5 (Figure 1).

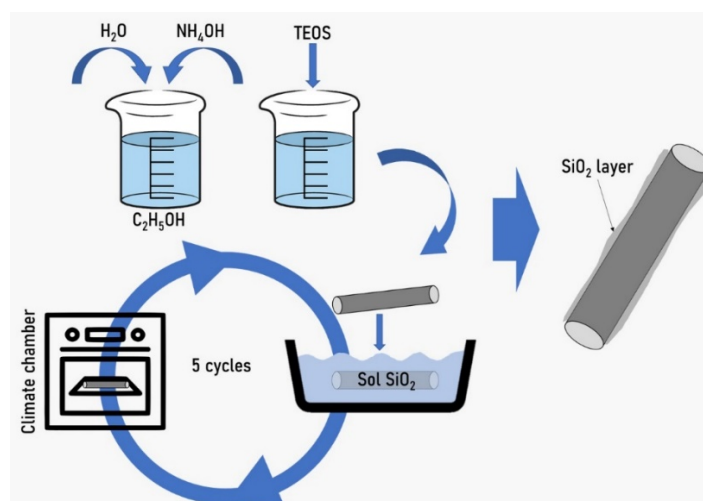


**Figure 1.** Scheme of formation of a nanostructured coating by SiO<sub>2</sub> sol deposition.

2. The sequential immersion method, based on alternating stages of applying tetraethoxysilane and ammonia solution ( $T = 25\text{ °C}$ ;  $\tau = 1\text{ min}$ ) to the surface of ABE wire [32]. After each stage of immersion, the ABE wire samples were dried in a drying chamber Oven 125 (“IKA”, Germany) at 150 °C for 10 min. To apply the next layer, the operation was repeated. The number of layers varied from 1 to 5 (Figure 2). When the wire is sequentially immersed in a solution of tetraethoxysilane and ammonium hydroxide, a layer of silicon dioxide is formed in accordance with the reaction:

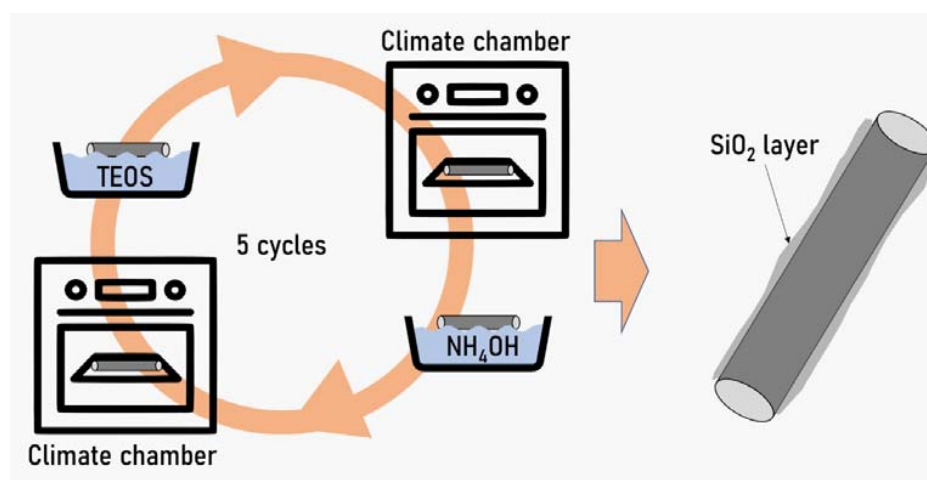


**Figure 2.** Scheme of formation of a nanostructured coating by sequential immersion in tetraethoxysilane and ammonia.

#### Research Methods

Measurements of the size and zeta potential of colloidal SiO<sub>2</sub> particles were carried out by acoustic and electroacoustic spectroscopy methods in the DT-1202 analyzer (“Dispersion Technology” Inc., Bedford Hills, NY, USA).

The microstructure and elemental composition of the surface of ABE wire samples were studied by scanning electron microscopy and energy dispersive microanalysis on a MIRA-LMH scanning electron microscope (Tescan, Brno, Czech Republic) with the AZtecEnergy Standard/X-max 20 (standard) elemental composition determination system (Tescan, Brno, Czech Republic) [33].

The study of the structural and mechanical properties of coated wires were carried out on a universal testing machine LabTest 6 (LLC “LABTEST”, Moscow, Russia) using DOLI Test & Motion software (LLC “LABTEST”, Moscow, Russia). Samples of ABE wires were subjected to a tensile test in static loading mode.

To measure the wetting contact angle, we prepared Ø 10 mm aluminum plates, the composition of which corresponded to the composition of the ABE wire. A nanostructured coating based on oxide materials was deposited on a part of the plates by consecutive immersion. The other part of the plates was treated with SiO<sub>2</sub> nanoparticles sol. A series of samples with a different number of application cycles of the oxide material-based nanostructured coating was prepared. The number of cycles varied from 1 to 5. The application of a drop of distilled water onto the experimental coating was carried out by an automatic micropipette; the wetting contact angle was measured using the LAUDA Scientific Surface Analyzer 100 device (“LAUDA DR. R. WOBSE” GmbH & CO. KG, Lauda-Königshofen, Germany).

The determination of the effectiveness of oxide coatings under laboratory conditions was carried out in the climate chamber EVCLIM KGH-250 (LLC “ERSTVAK”, Moscow, Russia). Three series of wire samples were placed in a climate chamber at 98% humidity and −40 °C temperature for 24 h; one of the samples was treated with a nanostructured oxide coating developed by sequential immersion in a solution of tetraethoxysilane and ammonia (5 layers); the second sample was coated by immersion in SiO<sub>2</sub> nanoparticle sol (5 layers); and the third sample was an uncoated wire (control sample). Then, the samples were removed from the climate chamber and the amount of ice formed was recorded.

All studies were carried out in a five-fold repetition ( $n = 5$ ). Statistical data processing was carried out in the Statistica 10.0 software (Statsoft, Tulsa, OK, USA). Graphical data processing was carried out in the Origin software (OriginLab, Northampton, MA, USA).

The analysis of the effect of the nanostructured coating on the high-frequency signal was carried out experimentally. The test was conducted on a test bench consisting of a PCIe-6351 signal generation and data acquisition module with a BNC-2120 terminal generating a frequency signal, using the National Instruments LabVIEW software package (“National Instruments” Inc., Austin, TX, USA) [34]. Figure 3 shows the connection diagram of this module with an ABE wire core. Using LabVIEW software, we also developed and wrote a program for the correct operation of the PCIe-6351 module with the BNC-2120 terminal.

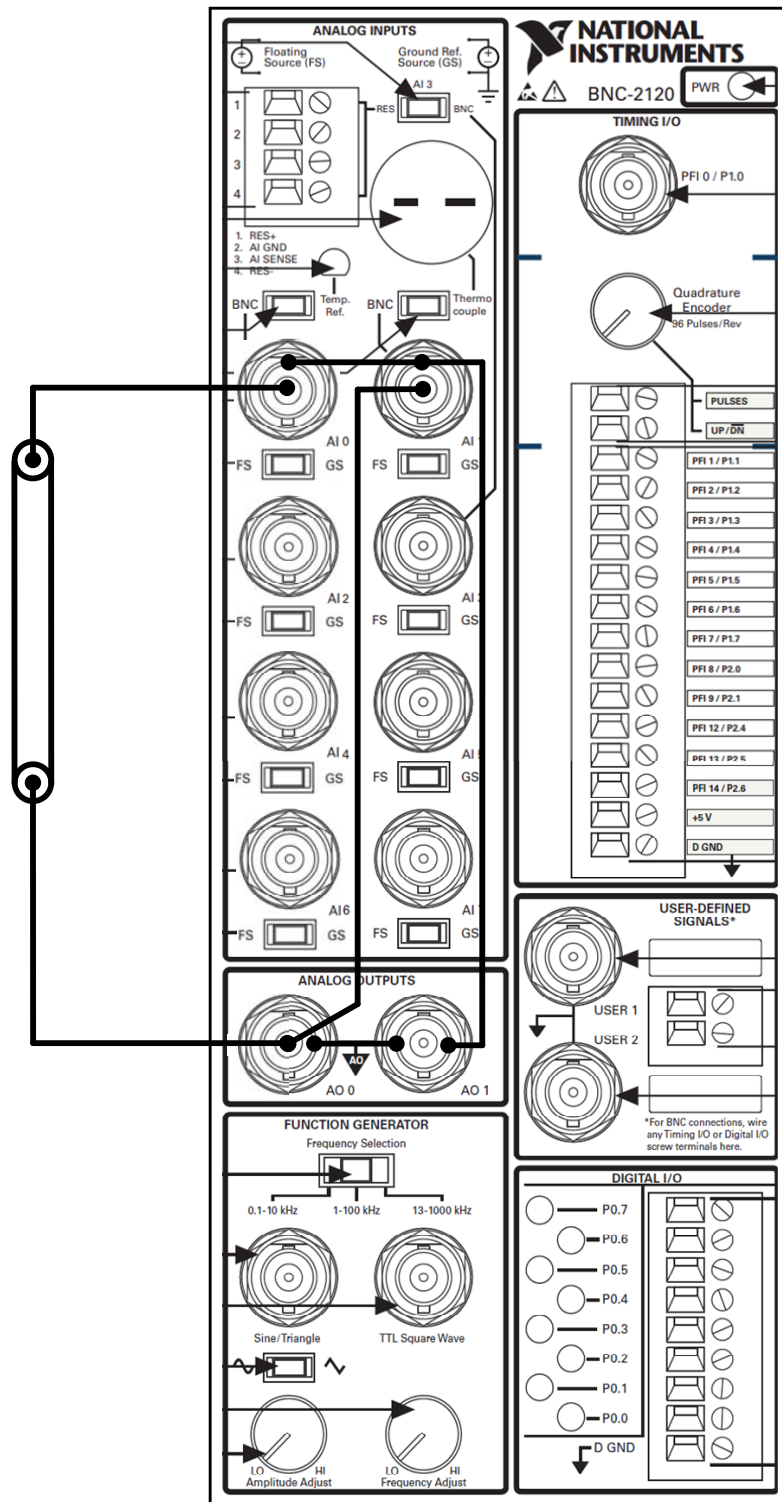


Figure 3. Connection diagram of the BNC-2120 module with ABE wire.

The measuring equipment used operates under the control of a program for generating voltage signals of a given shape, amplitude, and frequency, and measuring voltage waveforms, performed in the LabVIEW graphics programming environment, controls the hardware via the DAQmx driver. We used the method of direct estimation of the measured values of stresses at the ends of the experimental sample. Applying the generated voltage to one end of the wire sample, its value is measured at the connection point and at the opposite end of the sample. The voltage is generated with the specified parameters of amplitude, frequency, and initial phase. The measurement of voltage signals is performed continuously for 1 s and is recorded as an array of instantaneous values with a sampling frequency exceeding the frequency of the generated signal by an order of magnitude.

The images of the block diagram panel associated with the program are shown in Figures 4 and 5. Figure 4 shows the first part of the program code for managing the data generation and collection device. The first is the configuration of the analog voltage signal generation channel with the specified parameters of the minimum and maximum levels and the number of the generation channel. Next, the parameters of the continuous signal generation mode are set, as is the number of samples per unit time describing the signal and the selection of the clock source of the signal generator. Figure 5 illustrates the second part of the generation device control code. All operations of this part are performed in a loop by condition and contain three stages. The first one is aimed at forming a sequence of values describing the signal of the required shape, frequency, and amplitude. Then, the generated data array is loaded into the clipboard of the digital-to-analog converter, and the final action is the start of signal generation. When the cycle stops on demand or when an error occurs, generation stops and all settings of the generation device are cleared.

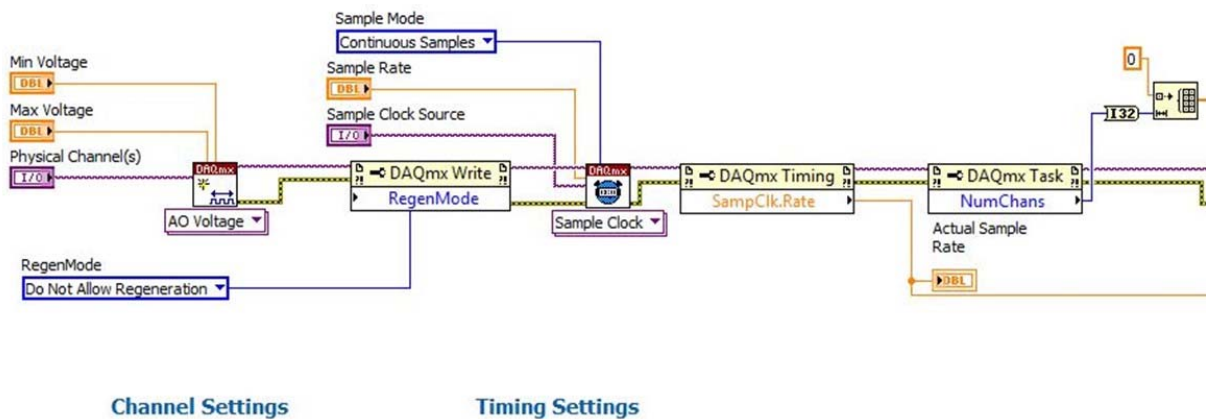


Figure 4. The first part of the block diagram panel.

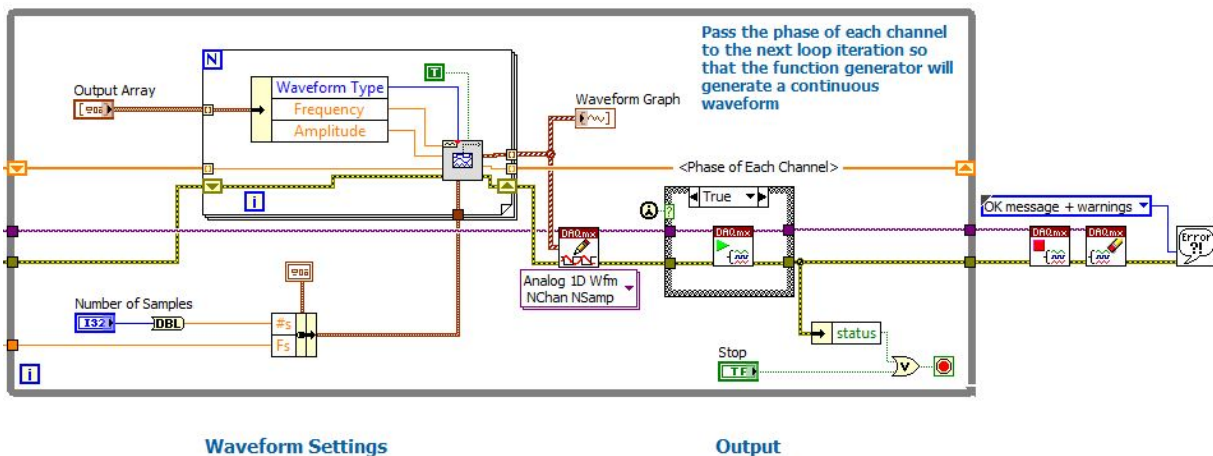


Figure 5. The second part of the block diagram panel.

To study the effect of the nanostructured coating on the high-frequency signal, the method of direct estimation of the measured values of stresses at the ends of the experimental sample was used. By applying the generated voltage to one end of the wire sample, its value can be measured at the connection point and at the opposite end of the sample. The voltage is generated with the specified parameters of amplitude, frequency, and initial phase. Voltage signals are measured continuously for 1 s and recorded as an array of instantaneous values with a sampling frequency exceeding the frequency of the generated signal by an order of magnitude. Accordingly, the voltage waveforms at the ends of the sample are measured. Then, the effective voltage values ( $U_1$  and  $U_2$ ) and voltage frequencies ( $f_1$  and  $f_2$ ) are determined, as well as the voltage drop on the sample  $\Delta U$ , as the voltage difference ( $U_1 - U_2$ ). The instrumental measurement error was 1%.

### 3. Results and Discussion

#### 3.1. Study of $\text{SiO}_2$ Nanoparticles

The  $\text{SiO}_2$  nanoparticles sol obtained by the Stober method was studied by acoustic and electroacoustic spectroscopy. The results of the  $\text{SiO}_2$  particles size determination and the nature of their size distribution are presented in Figure 6.

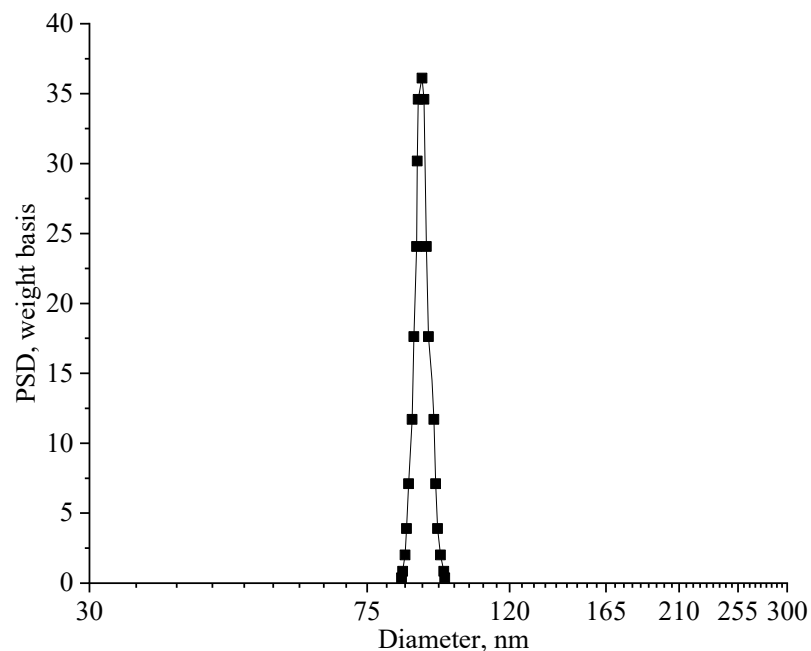


**Figure 6.** Histogram of  $\text{SiO}_2$  nanoparticle size distribution.

As can be seen in Figure 4, the distribution of  $\text{SiO}_2$  nanoparticles has a unimodal character; the average size of silicon oxide particles is  $90 \pm 12$  nm (the value of the average hydrodynamic radius  $\pm$  standard deviation). A silicon oxide particle has a small negative charge equal to  $-0.14$  mV.

#### 3.2. Investigation of the Process of Applying Nanostructured Coatings

The synthesized  $\text{SiO}_2$  nanoparticles sol was applied to the ABE wire surface. During the experiment, we prepared five groups of ABE wire with a different number of layers of  $\text{SiO}_2$  nanoparticles on the surface. Each group contained five samples. After each  $\text{SiO}_2$  nanoparticles application cycle, the samples were dried and weighed on analytical scales. Figure 7 shows a histogram of the relative mass variation (%) of the samples as a function of the number of  $\text{SiO}_2$  nanoparticles layers deposited.

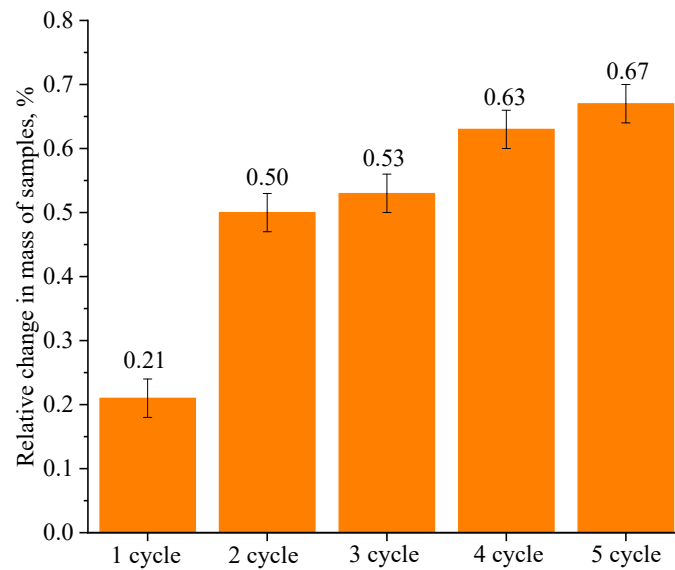


**Figure 7.** Relative change in the mass of ABE wire samples treated with SiO<sub>2</sub> nanoparticles sol.

As can be seen in Figure 7, after each cycle, the mass of the samples increased by 0.13% on average.

In the second part of the experiment, the protective coating was applied by sequential immersion in tetraethoxysilane and a 25% aqueous ammonia solution. Before the first tetraethoxysilane application cycle, the ABE wire samples were washed with distilled water and dried.

During the experiment, five groups of ABE wire samples with different contents of silicon oxide layers were obtained. Each group contained five samples. After each application cycle, the samples were dried at a temperature of 150 °C and weighed. According to the weighing results, the variation of the mass from the samples in relation to the initial mass of the ABE wire was determined. Figure 8 shows the dependence of the relative change in the mass of samples after each immersion cycle.

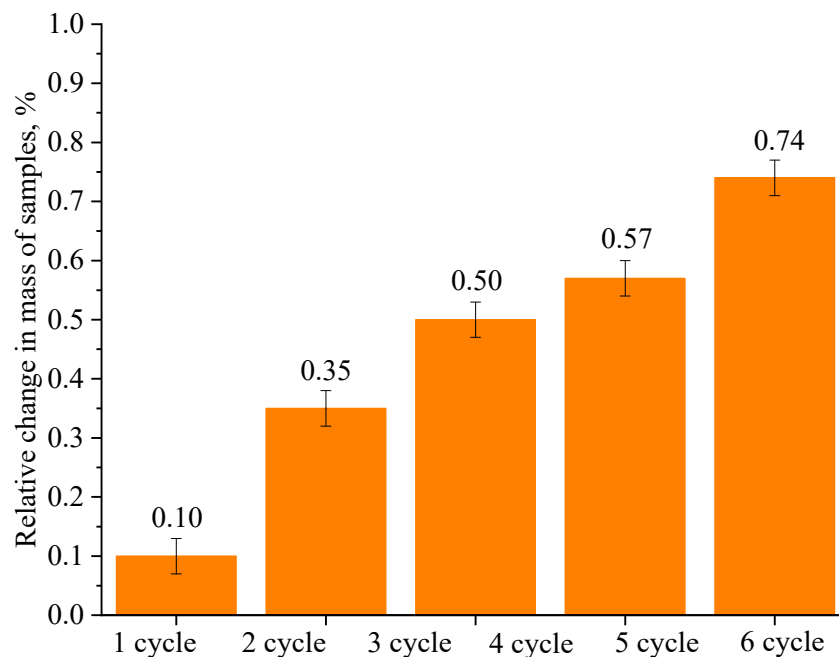


**Figure 8.** Relative change in the mass of ABE wire samples treated with a hydrophobic coating by sequential immersion method.

As can be seen in Figure 8, the average mass of samples after each cycle increased by 0.15%. After the application of five layers of protective coating, the relative change in the weight of the ABE wire does not exceed 1%. In more detail, the mechanical effect of additional weight due to the application of a nanostructured coating is analyzed in Section 3.8.

A comparative analysis of the change in the mass of ABE wires after the application of protective coating in two ways showed that the mass of samples treated with SiO<sub>2</sub> nanoparticles sol changes faster after the third cycle, and the mass of samples treated with a protective coating applied by the sequential immersion method changes faster after the fourth cycle. It is important to note that when applying a single coating layer, the largest change in the mass of the sample (0.21%) is observed in the case of using SiO<sub>2</sub> nanoparticles sol.

In the third stage of the experiment, we analyzed the elemental composition of the ABE wire samples using a Tescan MIRA-LMH scanning electron microscope with the AZtecEnergy Standard/X-max 20 (standard) elemental composition determination system (Tescan, Brno, Czech Republic). Figure 9 shows the elemental composition spectrum of an electrical aluminum alloy of the ABE wire, and Table 2 shows the interpretation of the spectrum.

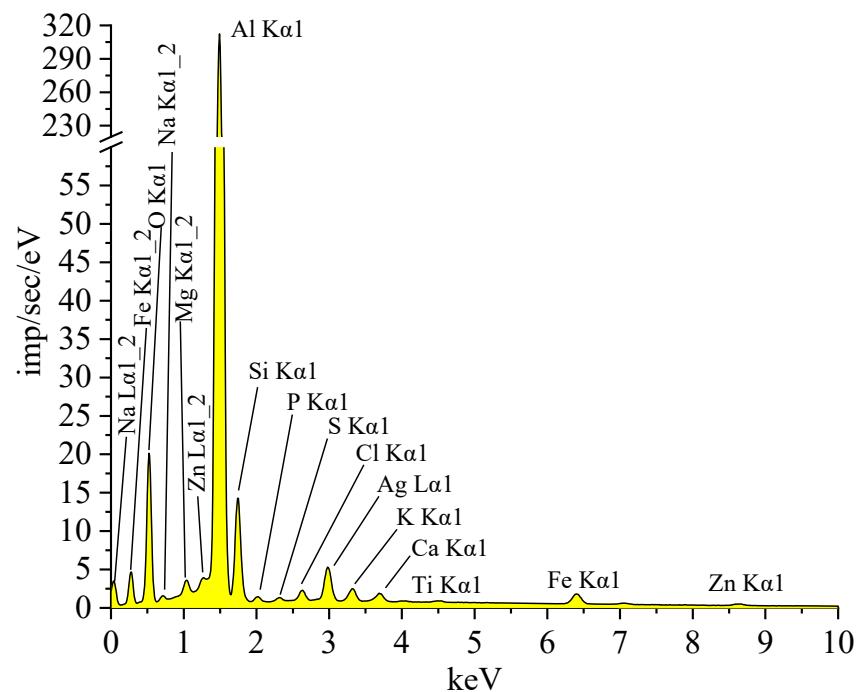


**Figure 9.** Spectrum of the elemental composition of an electrical aluminum alloy of one of the ABE wire samples.

**Table 2.** Interpretation of the spectra of the elemental composition of an electrical aluminum alloy of the ABE wire samples.

Element	Type of Line	Weight, %	Sigma Weight, %	Content of Atom, %
C	K series	14.72 ± 0.17	0.54	25.75 ± 0.21
O	K series	18.60 ± 0.23	0.13	24.42 ± 0.23
Na	K series	0.33 ± 0.01	0.01	0.30 ± 0.01
Mg	K series	0.18 ± 0.05	0.01	0.15 ± 0.01
Al	K series	56.19 ± 0.42	0.36	43.73 ± 0.37
Si	K series	4.78 ± 0.07	0.03	3.57 ± 0.06
P	K series	0.15 ± 0.01	0.01	0.10 ± 0.01
S	K series	0.15 ± 0.01	0.01	0.10 ± 0.01
Cl	K series	0.46 ± 0.02	0.01	0.27 ± 0.02
K	K series	0.70 ± 0.02	0.01	0.38 ± 0.02
Ca	K series	0.45 ± 0.01	0.01	0.24 ± 0.01
Ti	K series	0.09 ± 0.01	0.01	0.04 ± 0.01
Fe	K series	1.46 ± 0.04	0.02	0.55 ± 0.04
Zn	K series	0.48 ± 0.03	0.02	0.15 ± 0.02
Ag	L series	1.26 ± 0.02	0.02	0.24 ± 0.02
Summ:	-	100.00	-	100.00

Data presented are the mean of five repetitions ( $n = 5$ ) ± standard error.

The interpretation of the elemental composition spectrum showed that the aluminum alloy contains C, O, Na, Mg, Al, Si, P, S, Cl, K, Ca, Ti, Fe, Zn, and Ag. The sample contains 43.73 ± 0.37% (atom.) aluminum, 3.57 ± 0.06% (atom.) silicon, 0.15 ± 0.01% (atom.) magnesium, 0.04 ± 0.01% (atom.) titanium, and 0.55 ± 0.04% (atom.) iron, which corresponds to the composition of the ABE grade aluminum alloy according to GOST 839-80. The presence of elements such as carbon, oxygen, sodium, sulfur, phosphorus, and zinc, which are not declared for ABE wire in GOST 839-80, can be explained by contamination on the wire surface.

Table 3 shows the elemental composition of ABE wire samples with different numbers of layers of protective coating applied by the method of sequential immersion in tetraethoxysilane and ammonia solution.

From the analysis of the data presented in Table 3, we can draw the following conclusions:

- (1) after the application of a protective coating on the wire surface, the content of silicon and oxygen in the sample starts to increase;
- (2) with the increase of the number of layers of protective coating, the silicon and oxygen content in the sample composition increases and the aluminum content decreases. The decrease in the aluminum content is associated with an increase in the silicon oxide layer on the surface of the samples, which covers the surface of the aluminum wire and does not allow the use of a scanning electron microscope to determine the aluminum content on the surface of the samples.

**Table 3.** The ratio of elements (% atom.) present in the samples prepared with sequential immersion method.

Elements	Content of Atom, %					
	Control	1 Layer	2 Layers	3 Layers	4 Layers	5 Layers
C	25.75 ± 0.21	23.44 ± 0.31	9.72 ± 0.08	10.39 ± 0.05	9.21 ± 0.05	14.48 ± 0.07
O	24.42 ± 0.23	16.17 ± 0.05	38.64 ± 0.13	36.01 ± 0.21	43.04 ± 0.14	46.95 ± 0.27
Al	43.73 ± 0.37	57.1 ± 0.21	37.8 ± 0.26	40.43 ± 0.24	29.36 ± 0.28	16.7 ± 0.15
Si	3.57 ± 0.06	3.16 ± 0.05	13.56 ± 0.10	12.87 ± 0.05	18.09 ± 0.18	21.68 ± 0.14
K	0.38 ± 0.02	-	-	-	-	-
Ca	0.24 ± 0.01	-	-	-	-	-
Ti	0.04 ± 0.01	-	-	-	-	-
Fe	0.55 ± 0.04	0.13 ± 0.01	0.14 ± 0.01	0.18 ± 0.01	0.14 ± 0.01	0.13 ± 0.02
Zn	0.15 ± 0.02	-	-	0.02 ± 0.01	-	-
Ag	0.24 ± 0.02	-	0.05 ± 0.01	0.1 ± 0.01	0.15 ± 0.01	0.07 ± 0.01
Na	0.30 ± 0.01	-	0.08 ± 0.01	-	-	-
Mg	0.15 ± 0.01	-	-	-	-	-
P	0.10 ± 0.01	-	-	-	-	-
S	0.10 ± 0.01	-	-	-	-	-
Cl	0.27 ± 0.02	-	-	-	-	-

Table 4 shows the results of determining the elemental composition of ABE wire with a different number of layers of protective coating applied by the method of immersion of samples in SiO<sub>2</sub> nanoparticles sol.

**Table 4.** The ratio of elements (% atom.) present in the samples prepared with the method of immersion of samples in SiO<sub>2</sub> nanoparticles sol.

Elements	Control	1 Layer	2 Layers	3 Layers	4 Layers	5 Layers
C	25.75 ± 0.21	15.56 ± 0.18	23.69 ± 0.13	12.7 ± 0.12	10.19 ± 0.21	14.2 ± 0.14
O	24.42 ± 0.23	13.47 ± 0.13	25.73 ± 0.20	25.1 ± 0.19	31.82 ± 0.14	37.8 ± 0.28
Al	43.73 ± 0.37	67.21 ± 0.38	39.81 ± 0.37	55.1 ± 0.34	42.78 ± 0.23	30.6 ± 0.21
Si	3.57 ± 0.06	3.54 ± 0.12	9.49 ± 0.09	6.76 ± 0.07	13.5 ± 0.06	15.8 ± 0.05
K	0.38 ± 0.02	-	0.22 ± 0.02	-	-	0.09 ± 0.01
Ca	0.24 ± 0.01	-	0.05 ± 0.01	-	0.11 ± 0.01	0.09 ± 0.01
Ti	0.04 ± 0.01	-	-	-	1.15 ± 0.03	0.78 ± 0.03
Fe	0.55 ± 0.04	0.14 ± 0.01	0.16 ± 0.01	0.17 ± 0.01	0.12 ± 0.01	0.12 ± 0.01
Zn	0.15 ± 0.02	-	0.02 ± 0.01	0.02 ± 0.01	0.02 ± 0.01	0.02 ± 0.01
Ag	0.24 ± 0.02	-	0.21 ± 0.02	-	0.29 ± 0.03	0.24 ± 0.02
Na	0.30 ± 0.01	0.05 ± 0.02	0.41 ± 0.01	0.09 ± 0.01	-	0.36 ± 0.01
Mg	0.15 ± 0.01	-	-	-	-	-
P	0.10 ± 0.01	-	-	-	-	-
S	0.10 ± 0.01	-	0.04 ± 0.01	-	-	-
Cl	0.27 ± 0.02	-	0.16 ± 0.01	-	-	-

From the analysis of the results presented in Table 4, we can draw the following conclusions:

- (1) after applying the protective coating, the silicon and oxygen content increases with the number of layers of the protective coating, and the aluminum content decreases;

- (2) the oxygen and silicon content in the protective coating applied by immersion in silicon oxide sol is lower than that of the protective coating applied by sequential immersion in tetraethoxysilane and ammonia.

Next, we investigated the morphology of the surface of metallic aluminum by scanning electron microscopy (SEM). According to SEM micrographs (Figure 10), the surface structure of metallic aluminum is homogeneous and non-porous. With an increase in the resolution of the SEM, granules of crystalline aluminum oxide, of sizes from 0.3 to 0.45 microns, are clearly distinguishable on the surface.

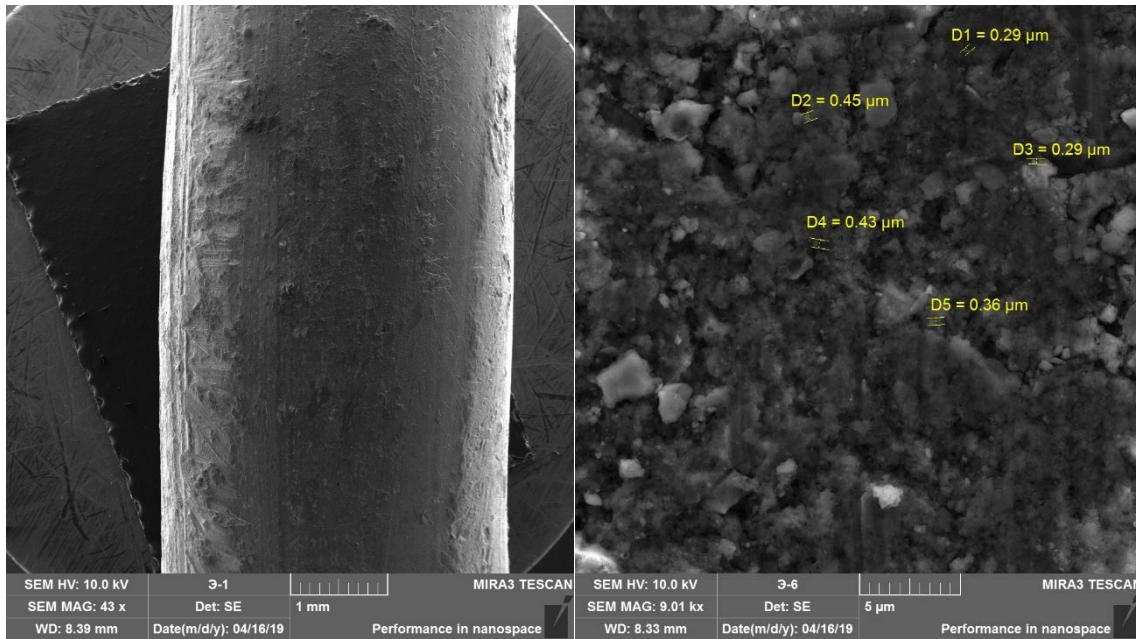


Figure 10. Micrography of the SEM surface of metallic aluminum.

Next, we studied the surface morphology of the experimental samples. Since the morphology of the samples' surface has a similar character, samples containing one, three, and five layers of protective coating on the surface were chosen as examples.

Figure 11 shows SEM micrographs of the surface of a sample containing one layer of protective coating applied by sequential immersion in tetraethoxysilane and ammonia.

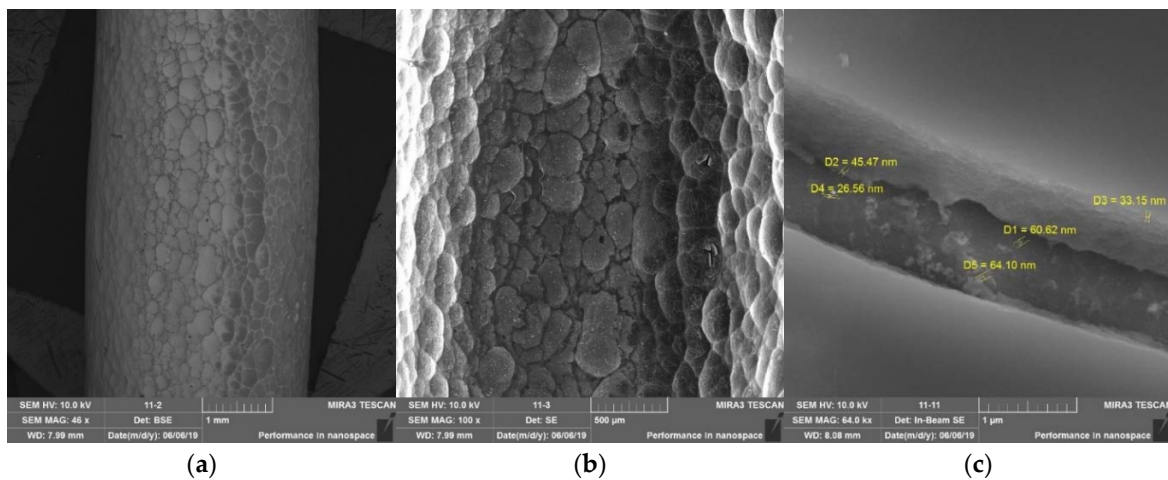
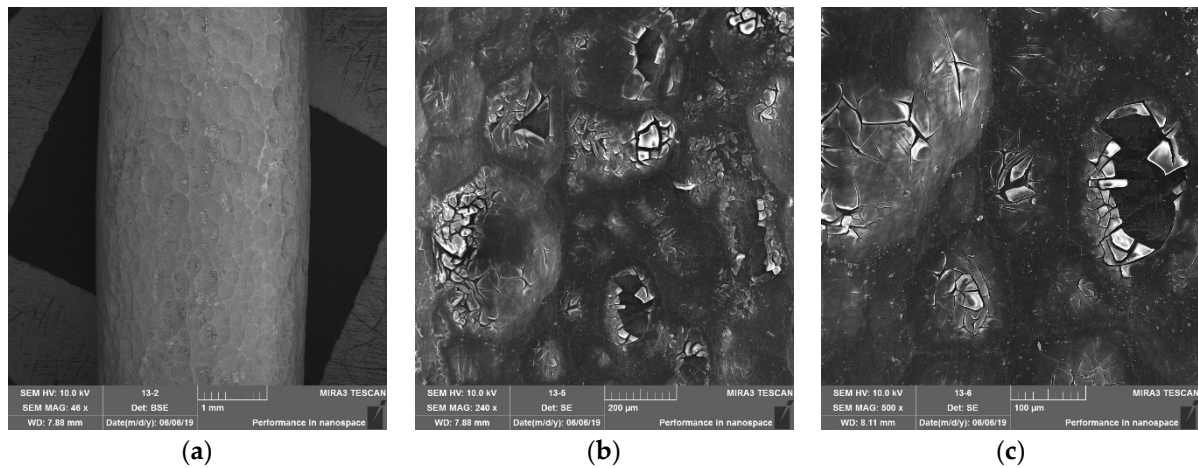


Figure 11. SEM micrographs of the surface of a sample containing one layer of protective coating applied by sequential immersion in tetraethoxysilane and ammonia. (a) zoom  $\times 46$ ; (b) zoom  $\times 100$ ; (c) zoom  $\times 64,000$ .

As can be seen from Figure 11, indentations are visible on the surface of the sample, and a silicon oxide film is present on the surface, which does not uniformly cover the surface of the sample. With a significant magnification, it can be seen that the film is not continuous, but consists of silicon oxide nanospheres with a diameter from 26 to 65 nm.

Figure 12 shows SEM micrographs of the surface of a sample containing three layers of protective coating applied by sequential immersion in tetraethoxysilane and ammonia.



**Figure 12.** SEM micrographs of the surface of a sample containing three layers of protective coating applied by sequential immersion in tetraethoxysilane and ammonia. (a) zoom  $\times 48$ ; (b) zoom  $\times 240$ ; (c) zoom  $\times 500$ .

As can be seen from Figure 12, after the application of the third layer of protective coating, the surface of the sample is more uniformly covered with a silicon oxide film. With magnification, it can be seen that the coating consists of flakes of various sizes.

Figure 13 shows SEM micrographs of the surface of a sample containing five layers of protective coating applied by sequential immersion in tetraethoxysilane and ammonia.

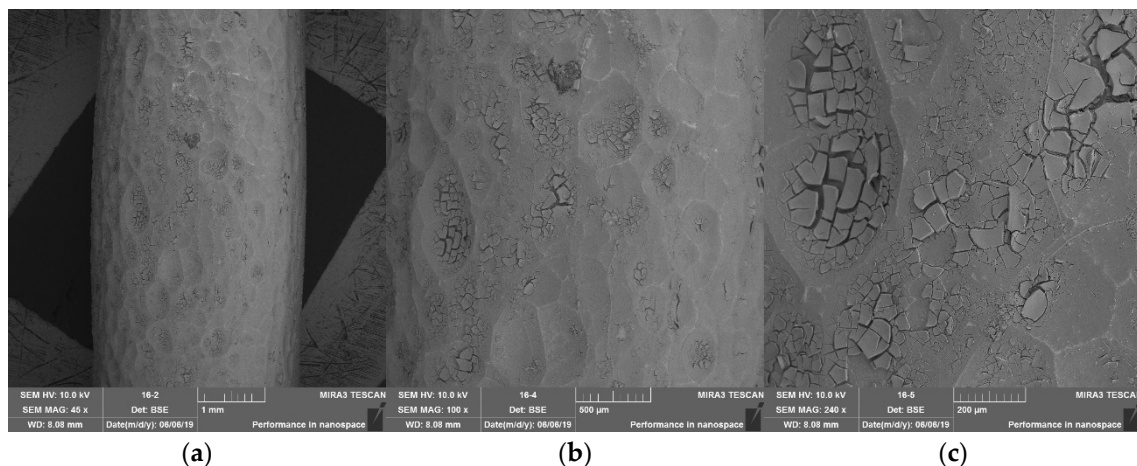


**Figure 13.** SEM micrographs of the surface of a sample containing five layers of protective coating applied by sequential immersion in tetraethoxysilane and ammonia. (a) zoom  $\times 45$ ; (b) zoom  $\times 100$ ; (c) zoom  $\times 240$ .

As can be seen from Figure 13, after the application of the five layers of protective coating, the surface of the sample is covered with a significant layer of silicon oxide. With magnification, it can be seen that in the pitting recesses, the oxide layer is denser, resulting in cracking of the coating.

Figures 14–16 show SEM micrographs of samples containing one, three, and five layers of protective coating, respectively, deposited by immersion in SiO<sub>2</sub> nanoparticles sol.

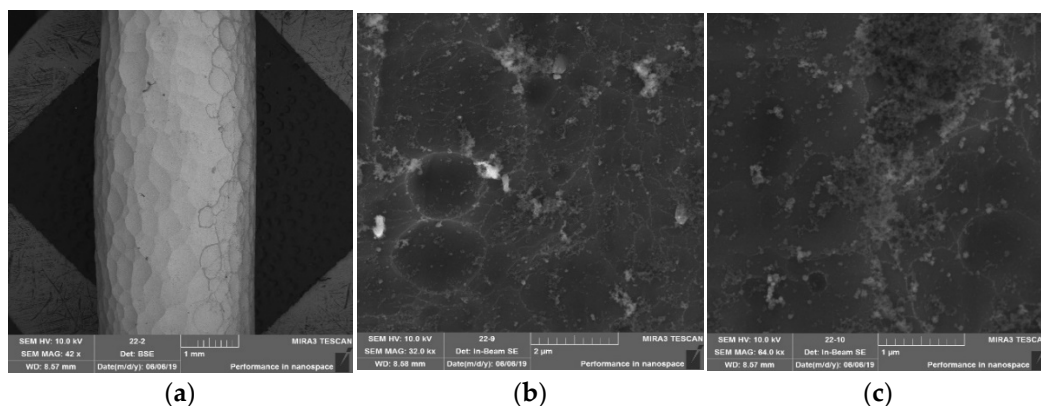


Figure 14. SEM micrographs of the surface of a sample containing one layer of protective coating applied by immersion in SiO<sub>2</sub> nanoparticles sol. (a) zoom ×42; (b) zoom ×32,000; (c) zoom ×64,000.

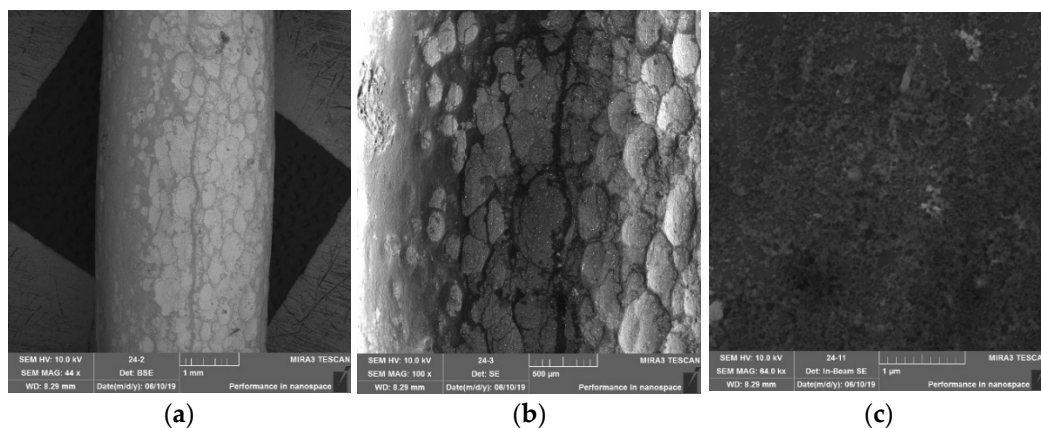


Figure 15. SEM micrographs of the surface of a sample containing three layers of protective coating applied by immersion in SiO<sub>2</sub> nanoparticles sol. (a) zoom ×44; (b) zoom ×100; (c) zoom ×64,000.

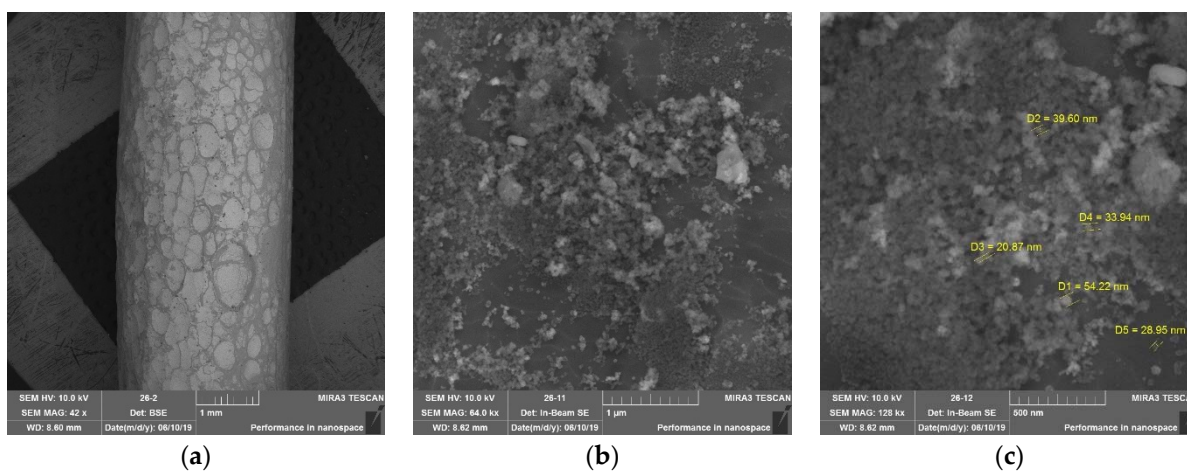


Figure 16. SEM micrographs of the surface of a sample containing five layers of protective coating applied by immersion in SiO<sub>2</sub> nanoparticles sol. (a) zoom ×42; (b) zoom ×64,000; (c) zoom ×128,000.

As can be seen from Figures 14–16, the surface of the ABE wire after applying layers of silicon oxide, regardless of the number of layers, is not uniformly coated. The degree

of coating increases with the number of cycles of silicon oxide application, but the main amount of aluminum oxide is decreased. With magnification, it can be seen that the coating is not homogeneous and consists of a silicon oxide nanosphere with different diameters ranging from 20 to 55 nm.

Thus, by the comparison of SEM micrographs of the surface of ABE wire samples with protective coating, we can conclude that the sequential immersion method in tetraethoxysilane and ammonia lead to denser and more uniform films of silicon oxide on the samples' surface, while immersion in SiO<sub>2</sub> nanoparticles sol does not allow for the achievement of the same degrees of surface coatings.

### 3.3. Investigation of Structural and Mechanical Properties of Nanostructured Coatings

In the next stage of research, we investigated the structural and mechanical characteristics of the coated wires on a universal testing machine LabTest 6. We used the DOLI Test & Motion software Version 3.5. As a result of the study, stretching diagrams were obtained for all samples. Three of them are shown in Figure 17.

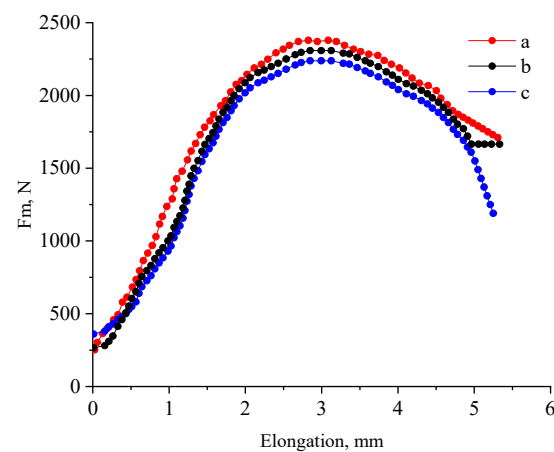


**Figure 17.** Stretching diagrams: (a) ABE wires treated by sequential immersion in tetraethoxysilane and ammonia (five cycles); (b) ABE wires treated by immersion in SiO<sub>2</sub> nanoparticles sol (five cycles); (c) uncoated wires (control sample).

Based on the analysis of tensile diagrams, the dependences of the tensile strength of the samples on the coating cycles were obtained and are presented in Figure 18.

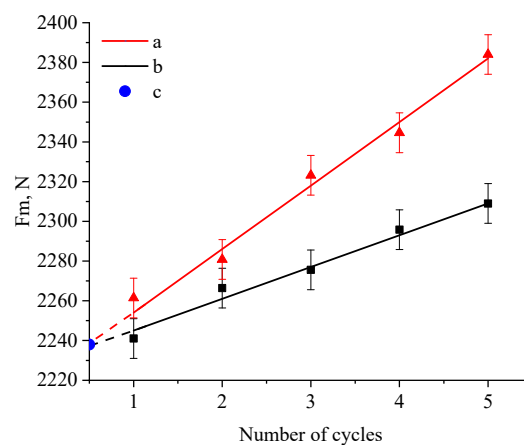


**Figure 18.** The dependences of the value of the tensile strength of samples on the number of coating cycles on the surface of the ABE wires: (a) ABE wires treated by sequential immersion in tetraethoxysilane and ammonia; (b) ABE wires treated by immersion in SiO<sub>2</sub> nanoparticles sol; (c) uncoated wires (control sample).

An analysis of the dependences obtained showed that the deposition of a nanostructured oxide coating on the wire increases the tensile strength of the material. It can be seen that for the sample coated by successive immersion in tetraethoxysilane and ammonia, the tensile strength was about 2385 N after five deposition cycles, and for the wire coated by immersion in the SiO<sub>2</sub> nanoparticle sol, the tensile strength was about 2305 N after five cycles. Thus, a coating deposited by successive immersion in tetraethoxysilane and ammonia exhibits increased strength, which is due to the uniform distribution of dense silicon oxide films on the surface of the samples. The results of investigation of structural and mechanical properties of nanostructured coatings are consistent with the results of the study of the microstructure of the surface of AEF wires. It is important to note that this material does not have a yielding area.

### 3.4. Investigation of the Effect of the Number of Nanostructured Coating Layers on the Wetting Contact Angle

In addition to studying the structural and mechanical properties of the samples, we analyzed the effect of the number of layers of oxide nanostructured coating on the wetting contact angle. The results of this study are presented in Figure 19.

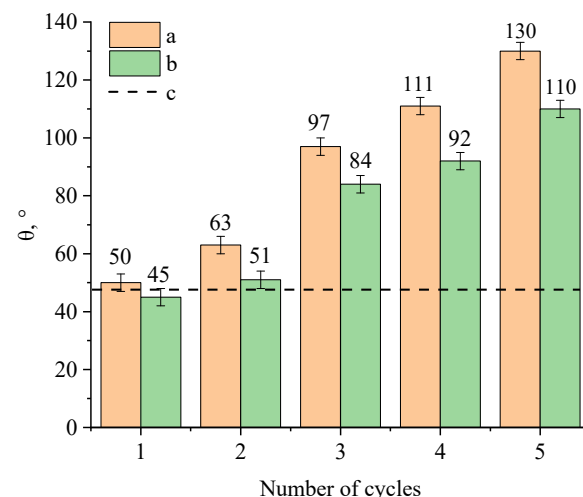


**Figure 19.** Dependence of the wetting contact angle on the number of application cycles: (a) ABE wires treated by sequential immersion in tetraethoxysilane and ammonia; (b) ABE wires treated by immersion in SiO<sub>2</sub> nanoparticles sol; (c) uncoated wires (control sample).

The analysis showed that the application of 1–2 layers of nanostructured oxide coating hardly affected the wetting contact angle. By applying 3–4 layers of oxide nanostructured coating, an increase in the wetting contact angle reached 90°, which indicates the formation of hydrophobic properties of the surface. In the samples with five layers of oxide nanostructured coating, the value of the wetting contact angle exceeded 120°, which is characteristic of materials with superhydrophobic properties. It should be noted that the sequential immersion method in tetraethoxysilane and ammonia achieves a larger wetting contact angle than the immersion method in SiO<sub>2</sub> nanoparticles sol.

### 3.5. Investigation of the Effectiveness of Nanostructured Coating in Critical Climatic Conditions

To study the effectiveness of the oxide nanostructured coating under model conditions, we placed three ABE wires in a climate chamber with humidity set at 98% and a temperature of −40 °C for 24 h. The first sample was treated with an oxide nanostructured coating developed by sequential immersion in tetraethoxysilane and ammonia; the second sample was treated by immersion in SiO<sub>2</sub> nanoparticle sol; and the third sample was a control. The result is shown in Figure 20.

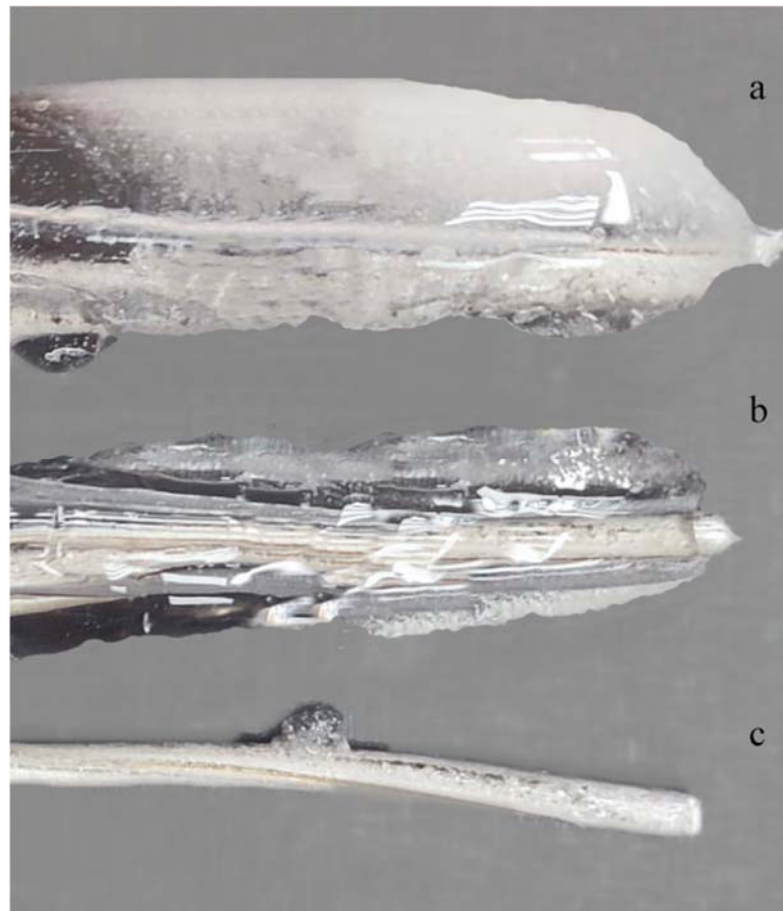


**Figure 20.** Photograph of ABE wire after climate chamber: (a) control sample (b) ABE wires treated by immersion in  $\text{SiO}_2$  nanoparticles sol (c) ABE wires treated by sequential immersion in tetraethoxysilane and ammonia.

As a result, the samples of the control group contained  $24.57 \pm 1.34$  g of ice, and the ABE wire samples treated by successive immersion in tetraethoxysilane and ammonia contained  $9.41 \pm 0.47$  g of ice. No ice crust formation was observed on the surface of ABE wire samples treated by sequential immersion in tetraethoxysilane and ammonia. The mass change in this series of samples before and after being placed in the climate chamber was  $0.52 \pm 0.13$  g.

### 3.6. Investigation of the Effect of a Nanostructured Coating on a High-Frequency Signal

As it is known, the protective coatings under development for overhead line wires can improve or deteriorate the bandwidth of high-frequency communication channels, as well as affect the electrical characteristics of the conductor. Therefore, we experimentally determined the change of the studied characteristics from the application method and the number of layers of oxide nanostructured coating [35–37].

The influence of the nanostructured coating on the high-frequency signal was determined in the National Instruments LabVIEW software package using the BNC-2120 module generating a frequency signal. During the experiment, we increased the frequencies from 50 Hz to 239,000 Hz and observed changes in voltage parameters with frequency changes. In the experiment, three types of wire were used. A wire without any application, a wire with the application of tetraethoxysilane and ammonia solution, and a wire with the application of  $\text{SiO}_2$  nanoparticles sol. Figure 21 shows the signal attenuation graphs at different frequencies for all ABE wire samples.

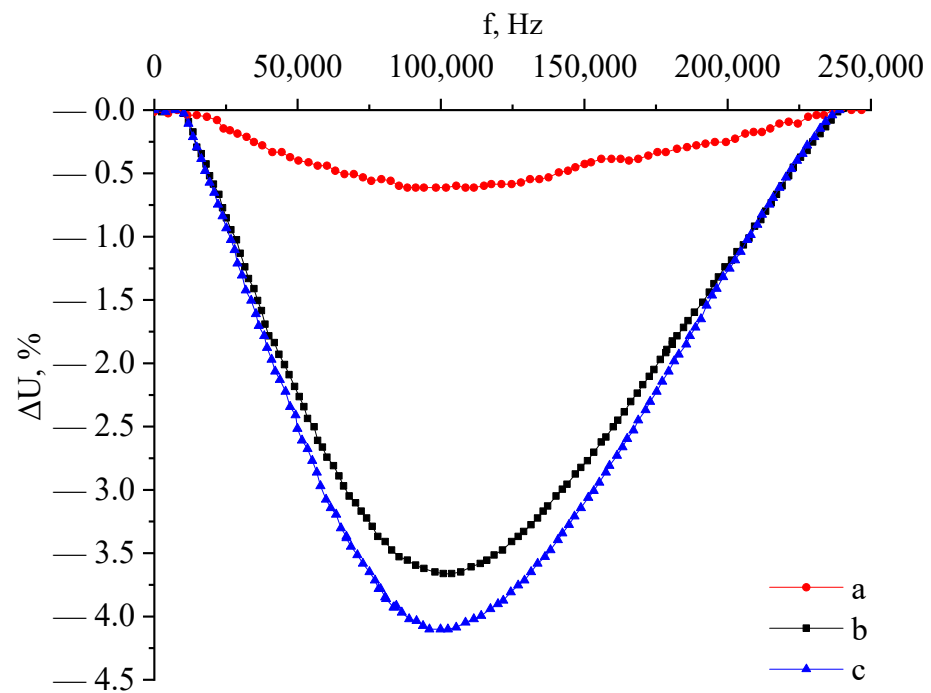


**Figure 21.** Graph of attenuation values for different frequencies: (a) ABE wires treated by sequential immersion in tetraethoxysilane and ammonia (five cycles); (b) ABE wires treated by immersion in SiO<sub>2</sub> nanoparticles sol (five cycles); (c) uncoated wires (control sample).

According to the obtained graph, it can be concluded that the wire coated with tetraethoxysilane and ammonia at a frequency of 100,000 Hz has the smallest voltage deviation. Thus, it can be said that covering the wire with tetraethoxysilane and ammonia results in a significant decrease in the magnitude of signal attenuation in the studied range.

### 3.7. Investigation of the Effect of a Nanostructured Coating on the Resistance of an ABE Wire

The effect of nanocoating on the resistance of the ABE wire was evaluated using the LabVIEW software package version 2022 Q3. The resistance of each aluminum core with a length of 30 cm was measured. Figure 22 shows the resistance values of ABE wire samples.

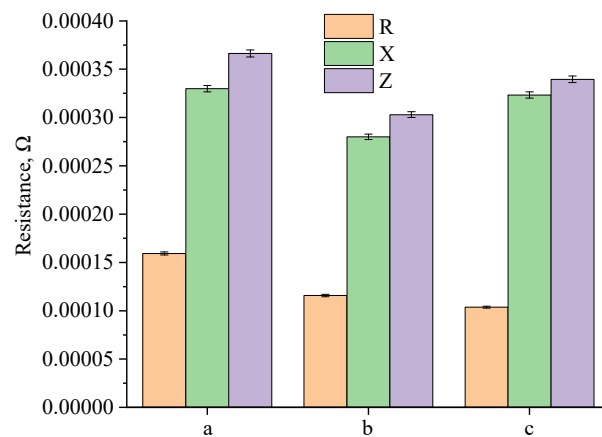


**Figure 22.** Resistance values of ABE wire samples: (a) ABE wires treated by sequential immersion in tetraethoxysilane and ammonia (five cycles); (b) ABE wires treated by immersion in SiO<sub>2</sub> nanoparticles sol (five cycles); (c) uncoated wires (control sample).

From the graphs (Figure 22), it can be seen that the reactance value (X) of the SiO<sub>2</sub>-coated ABE wire decreased by 18% compared to the control sample (from 0.000325 ± 0.00001

to  $0.000275 \pm 0.00001$ ), while the total resistance ( $Z$ ) also decreased by 13% (from  $0.00034 \pm 0.00001$  to  $0.00030 \pm 0.00001$ ), which leads to a decrease in active power losses and an improvement in the parameters of the electrical regime. At the same time, the highest resistance value was observed in the samples treated by tetraethoxysilane and ammonia. Based on these results, it can be concluded that power losses will be minimal at  $\text{SiO}_2$  coating application.

### 3.8. Investigation of the Effect of Nanostructured Coating on the Mechanical Characteristics of Power Lines

Since the applied substance has its own density and mass (the density of the applied substance  $g_0 = 2.65 \text{ kg/m}^3$  and the wall thickness of one coating layer  $b = 0.0002 \text{ mm}$ ), it is necessary to create conditions such that the sag, as well as distance to the ground, is within acceptable limits according to the electrical installation rules (Table 5) [35].

**Table 5.** Minimal vertical distance between overhead wires and the ground surface and industrial buildings and structures in a populated area.

Working Conditions of the Overhead Lines	The Minimal Distance (m), at an Overhead Lines Voltage (kV)							
	<20	<35	110	150	220	330	500	750
To the surface of ground	6	7	7	7.5	8	11	15.5	23
To industrial buildings and structures	3	3	4	4	5	7.5	8	12
Wire breakage in an adjacent span to the ground surface	5.0	5.5	5.5	5.5	5.5	6	-	-

The sagging arrow is the vertical distance between an imaginary horizontal line with the wire attachment point and the lowest point of the wire sagging in the span (Figure 23). The ground dimension is referred to as the smallest vertical distance between the lowest point of wire sag and the surface of the earth (rivers, lakes, railways, bridges, etc.). The span length is the distance along the line between two adjacent intermediate supports [38].

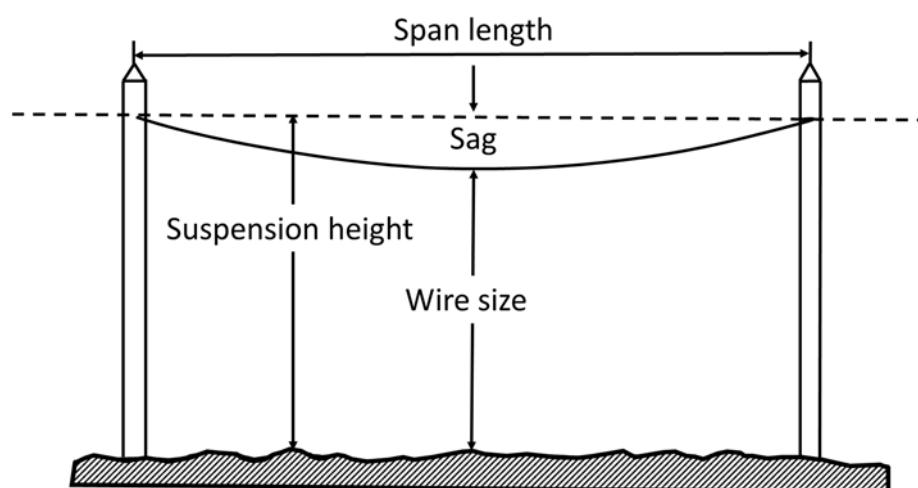


**Figure 23.** Scheme of the main terminology of the power line.

The wires are subjected to mechanical loads directed vertically (self-weight and ice) and horizontally (wind). Under the action of loads, tensile stresses occur in the metal [38]. A single load is a load that falls on 1 m of wire length. A specific unit load is a mechanical load uniformly distributed along the wire span, which falls on 1 m of the length of the wire and  $1 \text{ mm}^2$  of the wire cross-section [39]. These loads are calculated under the condition that the load is uniformly distributed and there are no wind gusts.

To calculate the dependence of the wire sag on the mass of the oxide nanostructured coating, we used an experimental intermediate support P-1TS-St-S (Table 6, Figure 24) [40].

**Table 6.** Structural dimensions and characteristics of the support.

Parameter	Meaning
Type of support	P-1TS-St-S
Total height of the support, m	25
Installation height of the traverse of phase A, m	19
Installation height of the traverse of phase B, m	19
Installation height of the traverse of phase C, m	23
Overall span length, m	400

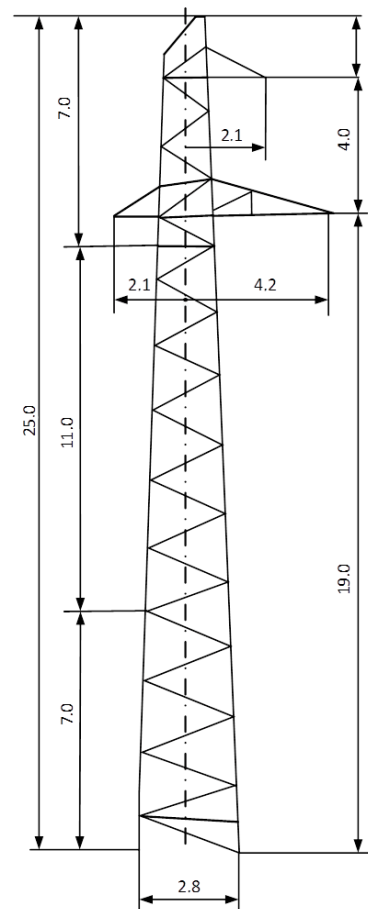


**Figure 24.** Steel intermediate support of 110 kV overhead line.

For the calculated theoretical experiment, we used the PS-70-V insulator corresponding to the voltage (Table 7) and the geometric dimensions of the line (Table 8)

**Table 7.** Physical and mechanical characteristics of the insulator.

Parameter	Value
Type of insulator	PS-70-B
Number of insulators	8
Electromechanical destructive load, daN	70
Total weight of insulators, kg	36
Construction height, m	1.35

**Table 8.** Geometric dimensions of the line.

Parameter	Value
Height of insulators, m	1.35
Height of the suspension of insulators of the wire 1 of the phase A circuit ( $h_{w1}$ ), m	19
Height of the suspension of insulators of the wire 1 of the phase B circuit ( $h_{w2}$ ), m	19
Height of the suspension of insulators of the wire 1 of the phase C circuit ( $h_{w3}$ ), m	23
Line size, m	7
Size margin, m	0.3

With data on the experimental support and the insulator, we can calculate the maximum possible sag. Calculations were carried out in accordance with the guidelines “Mechanical part of overhead power lines” and GOST 839-2019 “Non-insulated conductors for overhead power lines. Specifications” [41–43].

The sag is defined as:

$$f_{max} = h_{wire} - H_{size} - \Delta H_{size}, \quad (1)$$

where:

$H_{size}$ —Line size, m;

$\Delta H_{size}$ —Size margin, m;

$h_{wire}$ —Height of the wires to the insulators, which is equal to:

$$h_{wire} = h_w - \lambda, \quad (2)$$

where:

$\lambda$ —the constructive length of the insulators (1.35 m);

$h_w$ —the arithmetic mean of the heights of the centers of gravity of individual wires, which is equal to:

$$h_w = \frac{h_{w1} + h_{w2} + h_{w3}}{3} \quad (3)$$

$$h_w = \frac{19 + 19 + 23}{3} = 20.3 \text{ m}$$

Using Equation (2), we found the height of the wire fixation:

$$h_{wire} = 20.3 - 1.35 = 18.95 \text{ m.}$$

Further, according to Formula (1), we calculated the maximum allowable sag:

$$f_{max} = 18.95 - 7 - 0.3 = 11.65 \text{ m.}$$

The stress of the wire’s own weight, which depends on its material, can be determined by Formula (4).

$$\gamma_1 = \frac{G_0 \times 10^{-3}}{F_{cal}} \quad (4)$$

where:

$G_0$ —weight of 1 km of wire, kg/km;

$F_{cal}$ —the calculated cross-section of the wire, mm<sup>2</sup> (reference value) [44].

For experimental calculations, we used normative characteristics of the ABE wire (Table 9).

$$\gamma_1 = 471 \times 10^{-3} / 136.43 = 3.452 \times 10^{-3} \text{ daN/m} \cdot \text{mm}^2.$$

**Table 9.** Physical and mechanical characteristics of the ABE wire.

Physical and Mechanical Characteristics	Value
Diameter of the wire, mm	15.2
Calculated cross-section of the wire $F_{cal}$ , mm <sup>2</sup>	136.43
Specific weight of the wire $G_0$ , kg/km	471
Elastic modulus, $E \times 10^{-3}$ daN/mm <sup>2</sup>	8.25
Temperature coefficient of linear expansion $\alpha \times 10^6$ K <sup>-1</sup>	19.2
The normative permissible stress of the wire at the average annual temperature $\sigma_{tol}$ , daN/m·mm <sup>2</sup>	8.7

Knowing the load of the wire from its own weight, we calculated the sag using Formula (5).

$$f = \frac{\gamma_1 \times L_{size}^2}{8 \times \sigma_{tol}}, \quad (5)$$

where:

$L_{size}$ —overall span length (400 m);

$\sigma_{tol}$ —standard permissible wire voltage.

$$f = \frac{3.452 \times 10^{-3} \times 400^2}{8 \times 8.7} = 7.93 \text{ m.}$$

Thus, it can be concluded that the sag remains within the allowable range when loaded by the wire's own weight. We then calculated the load of a wire with N layers of oxide nanostructured coating (Formula (6)).

$$\gamma_2^N = \frac{g_0 \times \pi \times N \times b_{cal}(d + N \times b_{cal}) \times 10^{-3}}{F_{cal}}, \quad (6)$$

where:

$g_0$ —density of coating (2.65 kg/m<sup>3</sup>);

$b_{cal}$ —thickness of 1 layer;

$d$ —outer diameter of the ABE wire (15.2 mm);

$N$ —number of layers.

Then, we calculated the load of a wire with one layer of oxide nanostructured coating:

$$\gamma_2^1 = 2.65 \times 3.14 \times 1 \times 0.0002(15.2 + 1 \times 0.0002) \times 10^{-3} / 136.43 = 1.855 \times 10^{-7} \text{ daN/m}\cdot\text{mm}^2$$

The weight of the wire was also calculated with an increase in the amount of oxide nanostructured coating by one layer (Formula (7)).

$$\gamma_3^2 = \gamma_1 + \gamma_2^1, \quad (7)$$

$$\gamma_3^2 = 3.452 \times 10^{-3} + 1.855 \times 10^{-7} = 3.4522 \cdot 10^{-3} \text{ daN/m}\cdot\text{mm}^2.$$

From the calculations, it can be seen that one layer of the applied coating changes the load of  $0.0002 \cdot 10^{-3}$  daN/m·mm<sup>2</sup> (0.006%), which will not affect the increase in the sag, but how will the situation change if the overhead line wire is treated with 100 layers of oxide nanostructured coating? The following is a similar calculation using Formulas (6) and (7):

$$\gamma_2^{100} = \frac{2.65 \times 3.14 \times 100 \times 0.0002(15.2 + 100 \times 0.0002) \times 10^{-3}}{136.43} = 1.858 \times 10^{-5} \text{ daN/m}\cdot\text{mm}^2.$$

$$\gamma_3^{100} = 3.452 \times 10^{-3} + 1.858 \times 10^{-5} = 3.471 \times 10^{-3} \text{ daN/m}\cdot\text{mm}^2.$$

The value of sag according to Formula (5) will be:

$$f = \frac{3.471 \times 10^{-3} \times 400^2}{8 \times 8.7} = 7.98 \text{ m.}$$

Even with 100 layers of nanostructured oxide coating on the ABE wire, the load will increase by  $0.019 \times 10^{-3} \text{ daN/m} \cdot \text{mm}^2$  (0.55%), and the sag will only increase by 0.05 m, which will also be absolutely not critical. In addition, we carried out calculations for a large number of hydrophobic coating layers.

#### 4. Conclusions

We have developed a nanostructured coating for the protection of the wires of power lines. Two methods of applying a nanostructured coating to the surface of the ABE wire were used in this work: the method of sequential immersion in a solution of tetraethoxysilane and ammonia, and the method of immersion in  $\text{SiO}_2$  nanoparticles sol. We have established that the method of sequential immersion in a solution of tetraethoxysilane and ammonia is optimal, which has the following advantages compared to the method of immersion in  $\text{SiO}_2$  nanoparticles sol:

- formation of denser and more homogeneous coatings, consisting of silicon oxide nanoparticles with a diameter from 26 to 65 nm;
- higher content of silicon ( $21.68 \pm 0.14\%$  compared to  $15.8 \pm 0.05\%$ ) and oxygen ( $46.95 \pm 0.27\%$  compared to  $37.8 \pm 0.28\%$ ) in samples of nanostructured coatings;
- higher tensile strength (2385 N compared to 2305 N);
- higher wetting contact angle ( $130^\circ$  compared to  $110^\circ$ );
- higher efficiency in critical climatic conditions (ice mass  $0.52 \pm 0.13$  compared to  $9.41 \pm 0.47 \text{ g}$ );
- lower voltage deviation at 100,000 Hz (0.5% compared to 3.5%).

The disadvantage of nanostructured coatings obtained by sequential immersion in a solution of tetraethoxysilane and ammonia is an increase in reactive and total resistance, which leads to a loss of power in transmission lines. The use of nanostructured coatings obtained by immersion in  $\text{SiO}_2$  nanoparticles sol allows for the reduction of the reactive resistance by 18% and the total resistance by 13% compared with the control sample.

The calculation of the sag and the mechanical effect of the additional weight of the nanostructured coating showed that the application of five layers of coating does not significantly affect the mechanical characteristics of power lines.

The data obtained will become the basis for the industrial introduction of a new type of hydrophobic coatings for wires intended for northern regions with extremely low seasonal temperatures.

**Author Contributions:** A.V.B.: conceptualization, methodology, and supervision; D.A.K.: conceptualization, methodology, and supervision; M.A.Y.: methodology and investigation; P.A.Z.: investigation and formal analysis; L.P.A.: methodology and investigation; V.N.V.: investigation and visualization; R.A.Z.: investigation and writing—original draft; A.A.K.: investigation; D.G.M.: investigation and software; A.B.G.: investigation and visualization; A.A.G.: validation, software, and investigation; N.V.L.: formal analysis and resources; E.N.K.: writing—review and editing and resources; V.N.G.: formal analysis and resources; M.A.K.: investigation; M.A.S.: writing—review and editing; A.A.N.: writing—review and editing and project administration.. All authors have read and agreed to the published version of the manuscript.

**Funding:** This research received no external funding.

**Institutional Review Board Statement:** Not applicable.

**Informed Consent Statement:** Not applicable.

**Data Availability Statement:** All data are available upon request to the corresponding author.

**Acknowledgments:** The authors are thankful to the reviewers for positive evaluation of the article, useful recommendations, and for the time devoted to reviewing our manuscript. The work was carried out using the equipment of the Center for Collective Use of the North Caucasus Federal University with financial support from the Ministry of Education and Science of Russia, unique project identifier RF—2296.61321x0029 (agreement No. 075-15-2021-687).

**Conflicts of Interest:** The authors declare that they have no known competing financial interests or personal relationships that could have appeared to influence the work reported in this paper.

## References

1. Farzaneh, M.; Savadjiev, K. Statistical Analysis of Field Data for Precipitation Icing Accretion on Overhead Power Lines. *IEEE Trans. Power Deliv.* **2005**, *20*, 1080–1087. [\[CrossRef\]](#)
2. Ruszczak, B.; Tomaszewski, M. Extreme Value Analysis of Wet Snow Loads on Power Lines. *IEEE Trans. Power Syst.* **2015**, *30*, 457–462. [\[CrossRef\]](#)
3. Laforte, J.L.; Allaire, M.A.; Laflamme, J. State-of-the-Art on Power Line De-Icing. *Atmos. Res.* **1998**, *46*, 143–158. [\[CrossRef\]](#)
4. Cerrai, D.; Koukoulou, M.; Watson, P.; Anagnostou, E.N. Outage Prediction Models for Snow and Ice Storms. *Sustain. Energy Grids Netw.* **2020**, *21*, 100294. [\[CrossRef\]](#)
5. Wang, F.; Li, C.; Lü, Y. Influence of Hydrophobic Coating on Ice Accretion on Aluminum Conductor. *Zhongguo Dianji Gongcheng Xuebao/Proc. Chin. Soc. Electr. Eng.* **2011**, *31*, 123–128.
6. Menini, R.; Farzaneh, M. Elaboration of Al<sub>2</sub>O<sub>3</sub>/PTFE Icephobic Coatings for Protecting Aluminum Surfaces. *Surf. Coat. Technol.* **2009**, *203*, 1941–1946. [\[CrossRef\]](#)
7. Yury, K.; Filippov, M.; Makarov, A.; Malygina, I.; Soboleva, N.; Fantozzi, D.; Andrea, M.; Koivuluoto, H.; Vuoristo, P. Arc-Sprayed Fe-Based Coatings from Cored Wires for Wear and Corrosion Protection in Power Engineering. *Coatings* **2018**, *8*, 71. [\[CrossRef\]](#)
8. Xu, X.; Zhang, Z.; Guo, F.; Yang, J.; Zhu, X.; Zhou, X.; Xue, Q. Fabrication of Bionic Superhydrophobic Manganese Oxide/Polystyrene Nanocomposite Coating. *J. Bionic Eng.* **2012**, *9*, 11–17. [\[CrossRef\]](#)
9. Qing, Y.; Zheng, Y.; Hu, C.; Wang, Y.; He, Y.; Gong, Y.; Mo, Q. Facile Approach in Fabricating Superhydrophobic ZnO/Polystyrene Nanocomposite Coating. *Appl. Surf. Sci.* **2013**, *285*, 583–587. [\[CrossRef\]](#)
10. Syafiq, A.; Vengadaesvaran, B.; Ahmed, U.; Rahim, N.A.; Pandey, A.K.; Bushroa, A.R.; Ramesh, K.; Ramesh, S. Facile Synthesize of Transparent Hydrophobic Nano- CaCO<sub>3</sub> Based Coatings for Self-Cleaning and Anti-Fogging. *Mater. Chem. Phys.* **2020**, *239*, 121913. [\[CrossRef\]](#)
11. Chen, X.; Zhu, Y.; Guo, Y.; Zhou, B.; Zhao, X.; Du, Y.; Lei, H.; Li, M.; Wang, Z. Carbonization Synthesis of Hydrophobic CaCO<sub>3</sub> at Room Temperature. *Colloids Surf. A Physicochem. Eng. Asp.* **2010**, *353*, 97–103. [\[CrossRef\]](#)
12. Li, W.; Wang, Y.; Feng, Y.; Wang, Q.; Xu, X.; Li, G.; Dong, G.; Jing, S.; Chen, E.; Fan, X.; et al. Fabrication of Robust Conductive and Superhydrophobic Coating Based on Carbon Nanotubes. *Mater. Res. Express* **2020**, *7*, 055009. [\[CrossRef\]](#)
13. De Volder, M.F.L.; Tawfik, S.H.; Baughman, R.H.; Hart, A.J. Carbon Nanotubes: Present and Future Commercial Applications. *Science* **2013**, *339*, 535–539. [\[CrossRef\]](#)
14. Polizos, G.; Winter, K.; Lance, M.J.; Meyer, H.M.; Armstrong, B.L.; Schaeffer, D.A.; Simpson, J.T.; Hunter, S.R.; Datskos, P.G. Scalable Superhydrophobic Coatings Based on Fluorinated Diatomaceous Earth: Abrasion Resistance versus Particle Geometry. *Appl. Surf. Sci.* **2014**, *292*, 563–569. [\[CrossRef\]](#)
15. Lee, S.G.; Ham, D.S.; Lee, D.Y.; Bong, H.; Cho, K. Transparent Superhydrophobic/Translucent Superamphiphobic Coatings Based on Silica-Fluoropolymer Hybrid Nanoparticles. *Langmuir* **2013**, *29*, 15051–15057. [\[CrossRef\]](#)
16. Shang, H.M.; Wang, Y.; Limmer, S.J.; Chou, T.P.; Takahashi, K.; Cao, G.Z. Optically Transparent Superhydrophobic Silica-Based Films. *Thin Solid Films* **2005**, *472*, 37–43. [\[CrossRef\]](#)
17. Mahadik, S.A.; Kavale, M.S.; Mukherjee, S.K.; Rao, A.V. Transparent Superhydrophobic Silica Coatings on Glass by Sol-Gel Method. *Appl. Surf. Sci.* **2010**, *257*, 333–339. [\[CrossRef\]](#)
18. Sivolapov, P.; Myronyuk, O.; Baklan, D.; Berehovyj, T. Formation of effective concentration of film forming superhydrophobic coatings based on silicon dioxide. *Technol. Audit. Prod. Reserves* **2021**, *3*, 59. [\[CrossRef\]](#)
19. Xu, L.; He, J. Fabrication of highly transparent superhydrophobic coatings from hollow silica nanoparticles. *Langmuir* **2012**, *28*, 7512–7518. [\[CrossRef\]](#)
20. Rosales, A.; Maury-Ramírez, A.; Gutiérrez, R.M.-D.; Guzmán, C.; Esquivel, K. SiO<sub>2</sub>@TiO<sub>2</sub> Coating: Synthesis, Physical Characterization and Photocatalytic Evaluation. *Coatings* **2018**, *8*, 120. [\[CrossRef\]](#)
21. Mazur, M.; Wojcieszak, D.; Kaczmarek, D.; Domaradzki, J.; Song, S.; Gibson, D.; Placido, F.; Mazur, P.; Kalisz, M.; Poniedzialek, A. Functional Photocatalytically Active and Scratch Resistant Antireflective Coating Based on TiO<sub>2</sub> and SiO<sub>2</sub>. *Appl. Surf. Sci.* **2016**, *380*, 165–171. [\[CrossRef\]](#)
22. Sirimahachai, U.; Ndiege, N.; Chandrasekharan, R.; Wongnawa, S.; Shannon, M.A. Nanosized TiO<sub>2</sub> Particles Decorated on SiO<sub>2</sub> Spheres (TiO<sub>2</sub>/SiO<sub>2</sub>): Synthesis and Photocatalytic Activities. *J. Sol-Gel Sci. Technol.* **2010**, *56*, 53–60. [\[CrossRef\]](#)
23. Radev, D.D.; Uzunov, I. Nanosized Silicon Carbide Obtained from Rice Husks. *Solid State Phenom.* **2010**, *159*, 153–156. [\[CrossRef\]](#)
24. Dou, W.; Wang, P.; Zhang, D.; Yu, J. An Efficient Way to Prepare Hydrophobic Antireflective SiO<sub>2</sub> Film by Sol-Gel Method. *Mater. Lett.* **2016**, *167*, 69–72. [\[CrossRef\]](#)

25. Farimani, M.H.R.; Shahtahmasebi, N.; Rezaee Roknabadi, M.; Ghows, N.; Kazemi, A. Study of Structural and Magnetic Properties of Superparamagnetic Fe<sub>3</sub>O<sub>4</sub>/SiO<sub>2</sub> Core–Shell Nanocomposites Synthesized with Hydrophilic Citrate-Modified Fe<sub>3</sub>O<sub>4</sub> Seeds via a Sol–Gel Approach. *Phys. E Low-Dimens. Syst. Nanostructures* **2013**, *53*, 207–216. [[CrossRef](#)]
26. Meng, X.; Qian, Z.; Wang, H.; Gao, X.; Zhang, S.; Yang, M. Sol-Gel Immobilization of SiO<sub>2</sub>/TiO<sub>2</sub> on Hydrophobic Clay and Its Removal of Methyl Orange from Water. *J. Sol-Gel Sci. Technol.* **2008**, *46*, 195–200. [[CrossRef](#)]
27. Pietrzyk, B.; Porębska, K.; Jakubowski, W.; Miszczak, S. Antibacterial Properties of Zn Doped Hydrophobic SiO<sub>2</sub> Coatings Produced by Sol-Gel Method. *Coatings* **2019**, *9*, 362. [[CrossRef](#)]
28. Parale, V.G.; Kim, T.; Lee, K.-Y.; Phadtare, V.D.; Dhavale, R.P.; Jung, H.-N.-R.; Park, H.-H. Hydrophobic TiO<sub>2</sub>–SiO<sub>2</sub> Composite Aerogels Synthesized via in Situ Epoxy-Ring Opening Polymerization and Sol-Gel Process for Enhanced Degradation Activity. *Ceram. Int.* **2020**, *46*, 4939–4946. [[CrossRef](#)]
29. Śmieszek, A.; Donesz-Sikorska, A.; Grzesiak, J.; Krzak, J.; Marycz, K. Biological Effects of Sol–Gel Derived ZrO<sub>2</sub> and SiO<sub>2</sub>/ZrO<sub>2</sub> Coatings on Stainless Steel Surface—In Vitro Model Using Mesenchymal Stem Cells. *J. Biomater. Appl.* **2014**, *29*, 699–714. [[CrossRef](#)]
30. Xu, S.; Jia, H.; Wang, C.; Zhao, W.; Wang, Y.; Yang, C.; Wu, H.; Zhu, J.; Wang, B.; Wang, Q. Low-Temperature Preparation of SiO<sub>2</sub>/Nb<sub>2</sub>O<sub>5</sub>/TiO<sub>2</sub>–SiO<sub>2</sub> Broadband Antireflective Coating for the Visible via Acid-Catalyzed Sol–Gel Method. *Coatings* **2020**, *10*, 737. [[CrossRef](#)]
31. Blinov, A.V.; Jasnaja, M.A.; Kravtsov, A.A.; Gvozdenko, A.A.; Raffa, V.V. Microstructure and Elemental Composition of Multicomponent Systems Based on Silicon, Titanium and Zirconium Oxides. *IOP Conf. Ser. Mater. Sci. Eng.* **2021**, *1029*, 012060. [[CrossRef](#)]
32. Gurav, A.B.; Xu, Q.; Lathe, S.S.; Vhatkar, R.S.; Liu, S.; Yoon, H.; Yoon, S.S. Superhydrophobic Coatings Prepared from Methyl-Modified Silica Particles Using Simple Dip-Coating Method. *Ceram. Int.* **2015**, *41*, 3017–3023. [[CrossRef](#)]
33. Tălu, Ș. *Micro and Nanoscale Characterization of Three Dimensional Surfaces. Basics and Applications*; Napoca Star Publishing House: Cluj-Napoca, Romania, 2015; pp. 21–27.
34. Elliott, C.; Vijayakumar, V.; Zink, W.; Hansen, R. National Instruments LabVIEW: A Programming Environment for Laboratory Automation and Measurement. *J. Lab. Autom.* **2007**, *12*, 17–24. [[CrossRef](#)]
35. Kurita, T.; Nishimori, Y.; Toshimitsu, F.; Muratsugu, S.; Kume, S.; Nishihara, H. Surface Junction Effects on the Electron Conduction of Molecular Wires. *J. Am. Chem. Soc.* **2010**, *132*, 4524–4525. [[CrossRef](#)] [[PubMed](#)]
36. Zhang, X.; Cotton, I.; Li, Q.; Rowland, S.M.; Emersic, C.; Lian, C.; Li, W. Experimental Verification of the Potential of Superhydrophobic Surfaces in Reducing Audible Noise on HVAC Overhead Line Conductors. *High Volt.* **2022**, *7*, 692–704. [[CrossRef](#)]
37. Arshad; Momen, G.; Farzaneh, M.; Nekahi, A. Properties and Applications of Superhydrophobic Coatings in High Voltage Outdoor Insulation: A Review. *IEEE Trans. Dielectr. Electr. Insul.* **2017**, *24*, 3630–3646. [[CrossRef](#)]
38. Brumsickle, W.E. Dynamic Sag Correctors: Cost-Effective Industrial Power Line Conditioning. *IEEE Trans. Ind. Appl.* **2001**, *37*, 212–217. [[CrossRef](#)]
39. Oluwajobi, F.; Ale, O.; Ariyanninuola, A. Effect of Sag on Transmission Line. *J. Emerg. Trends Eng. Appl. Sci.* **2012**, *3*, 627–630.
40. Rezaeva, M.A. Lightning Resistance Analysis of Overhead Power Lines on Composite Supports in Comparison with Overhead Lines on Traditional Supports. In Proceedings of the 2020 International Multi-Conference on Industrial Engineering and Modern Technologies (FarEastCon), Vladivostok, Russia, 6–9 October 2020; IEEE: Piscataway, NJ, USA, 2020; pp. 1–5.
41. GOST 839-2019; Non-Insulated Conductors for Overhead Power Lines. Specifications. USSR State Committee for Standards: Moscow, Russia, 2019; p. 21.
42. Popov, E.N. *Mechanical Part of Overhead Power Lines*; Amur State un-t: Blagoveshchensk, Russia, 1999.
43. Farzaneh, M.; Jakl, F.; Arabani, M.P.; Eliasson, A.J.; Fikke, S.M.; Gallego, A.; Haldar, A.; Isozaki, M.; Lake, R.; Leblond, L. *Systems for Prediction and Monitoring of Ice Shedding, Anti-Icing and De-Icing for Power Line Conductors and Ground Wires*; University of Huddersfield: Huddersfield, UK, 2010.
44. Faibisovich, D.L. *Electrical Network Design Handbook*; ENAS: Moscow, Russia, 2012.